



The interplay between thermodynamics and kinetics in the solid-state synthesis of layered oxides

Matteo Bianchini^{1,2,3,8}, Jingyang Wang^{1,2,8}, Raphaële J. Clément^{2,4}, Bin Ouyang^{1,2}, Penghao Xiao^{1,2}, Daniil Kitchaev⁴, Tan Shi^{1,2}, Yaqian Zhang^{1,2}, Yan Wang⁵, Haegyeom Kim^{1,2}, Mingjian Zhang⁶, Jianming Bai⁶, Feng Wang⁶, Wenhao Sun^{1,7}✉ and Gerbrand Ceder^{1,2}✉

In the synthesis of inorganic materials, reactions often yield non-equilibrium kinetic byproducts instead of the thermodynamic equilibrium phase. Understanding the competition between thermodynamics and kinetics is a fundamental step towards the rational synthesis of target materials. Here, we use in situ synchrotron X-ray diffraction to investigate the multistage crystallization pathways of the important two-layer (P2) sodium oxides $\text{Na}_{0.67}\text{MO}_2$ ($M = \text{Co}, \text{Mn}$). We observe a series of fast non-equilibrium phase transformations through metastable three-layer O3, O3' and P3 phases before formation of the equilibrium two-layer P2 polymorph. We present a theoretical framework to rationalize the observed phase progression, demonstrating that even though P2 is the equilibrium phase, compositionally unconstrained reactions between powder precursors favour the formation of non-equilibrium three-layered intermediates. These insights can guide the choice of precursors and parameters employed in the solid-state synthesis of ceramic materials, and constitutes a step forward in unravelling the complex interplay between thermodynamics and kinetics during materials synthesis.

Designing and synthesizing new materials with tailored properties are cumbersome tasks. When approaching materials synthesis, the thermodynamic phase diagram is often a general starting point. Guided by it, one should prepare precursors at a composition where a desired equilibrium phase is stable, and obtain it by holding the system under appropriate thermodynamic conditions (temperature and pressure) for a sufficiently long time. Both experimental and ab initio predicted phase diagrams are guiding tools for synthesis^{1–3}, yet they often become unreliable when reaction kinetics plays a major role. Notably, compounds predicted as thermodynamically stable often cannot be synthesized experimentally⁴, whereas metastable materials (that is, those higher in energy than the ground-state phases) are often observed during materials formation^{5–8}.

Several in situ studies of synthesis reactions^{9–18} have shown that the path towards the target phase often proceeds through multiple non-equilibrium intermediates. This pathway is important as long-lived metastable intermediates can persist as impurity phases in the final product or they can structurally template ensuing phase transformations^{13–15}. Although kinetic factors can be exploited to guide the outcome of specific reactions^{14,15}, currently no general guiding principles exist to predict or rationalize these pathways, which can be entirely thermodynamic or kinetic, or result from the intricate interplay of the two. Being able to account for and anticipate these metastable intermediates would represent a milestone in building a predictive theory of synthesis. This is especially important given the emergence of computational materials-by-design methods, which have dramatically increased the number of compelling materials to be experimentally investigated^{19–21}.

In this paper, we systematically explore the non-equilibrium formation pathways of layered Na metal oxides by means of in situ synchrotron X-ray diffraction (XRD) and ab initio computations. We chose these Na-based compounds due to their technological relevance as battery electrodes²², thermoelectrics²³ and superconducting materials²⁴, as well as for their structural complexity with many competing phases^{25–28}. The layered Na_xMO_2 structures form in two major polytypes, which can be distinguished by their oxygen stacking sequence and Na environments (Fig. 1b): P2, with a two-layer stacking; and O3 and P3, with a three-layer stacking. Symmetry breaking by secondary phenomena (for example, Na ordering, Jahn–Teller distortions) are indicated by primes (for example, O3'/P3'). Properties such as Na^+ mobility and electronic and thermal conductivities are highly dependent on the stoichiometry and structure of the Na_xMO_2 phase under consideration. For example, P2 phases are attractive Na-ion cathode materials exhibiting excellent Na^+ conductivity^{29,30}.

Understanding practical synthesis routes to these specific Na_xMO_2 structures is essential. The thermodynamic stability of different Na_xMO_2 polytypes varies with the Na content, x , as calculated in Fig. 1a, where the unprimed labels (O3/P3/P2) are used to designate the stacking regardless of whether the symmetry is further broken. In the Na_xCoO_2 system, the O3-type stacking exhibits octahedrally coordinated alkali and transition metals, and is the lowest energy phase at high sodiation; meanwhile at $x=0.67$, a two-layer structure with prismatically coordinated Na ions (P2) is the ground-state phase. Thus, although the density functional theory (DFT) energy differences are small, thermodynamic considerations imply that P2

¹Materials Sciences Division, Lawrence Berkeley National Laboratory, Berkeley, CA, USA. ²Department of Materials Science and Engineering, University of California, Berkeley, CA, USA. ³Battery and Electrochemistry Laboratory, Institute of Nanotechnology, Karlsruhe Institute of Technology (KIT), Eggenstein-Leopoldshafen, Germany. ⁴Materials Department, University of California Santa Barbara, Santa Barbara, CA, USA. ⁵Samsung Research America, Burlington, MA, USA. ⁶Brookhaven National Laboratory, Upton, NY, USA. ⁷Department of Materials Science and Engineering, University of Michigan, Ann Arbor, MI, USA. ⁸These authors contributed equally: Matteo Bianchini, Jingyang Wang. ✉e-mail: whsun@umich.edu; gceder@berkeley.edu

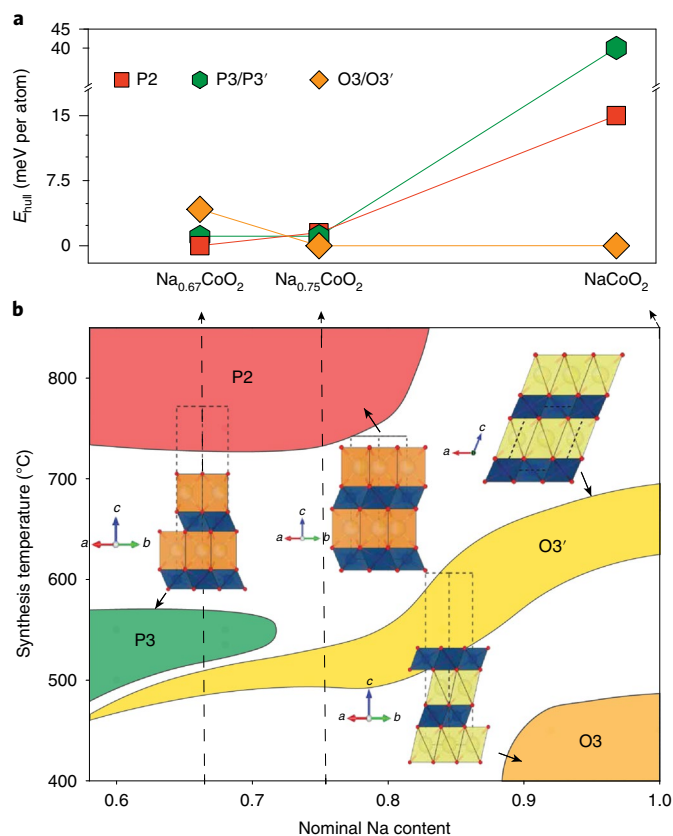


Fig. 1 | Predicted thermodynamic stability and experimentally observed synthetic accessibility of Na_xCoO_2 polytypes. **a**, Energy above the convex hull (E_{hull}) of the various polytypes of Na_xCoO_2 in their lowest-energy $\text{Na}/$ vacancy configuration at $x=0.67, 0.75$ and 1 , calculated with the DFT-SCAN meta-GGA functional⁴⁴. **b**, Sodium layered oxides Na_xCoO_2 experimentally stabilized as a function of their Na content x and of the temperature at which they are commonly synthesized in air. Coloured areas denoted by P2, P3, O3' and O3 are single-phase regions suggested by Lei et al.³¹, representing the literature before this work. The crystal structure of each polymorph is shown and labelled using the notation introduced by Delmas et al.²⁵: the letter stands for the type of Na environment (P, prismatic; O, octahedral), while the number describes the oxygen stacking (for example, in P2 Na ions occupy prismatic sites in between ABBA oxygen stacking). Blue units represent CoO_6 octahedral environments, yellow and orange units NaO_6 octahedral and prismatic environments, respectively. A prime symbol (for example, P3') indicates a monoclinic or orthorhombic distortion of the unprimed structure, typically due to Na ordering (or Jahn-Teller distortions for the Mn system). For example, a P3–P3' reversible transition occurs at 350–370 K (ref. 45). Note that in the computational results we use the unprimed notation for all structures (for example, O3' is O3) because the distinction is not very meaningful in the structures prepared for computations. For $x < 1$, Na-vacancy ordering in the DFT already breaks the symmetry of the O3 lattice and only a structure where the Na and vacancies are disordered (thereby re-establishing the equivalence of all Na sites) can have O3 symmetry.

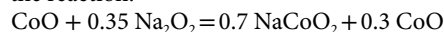
should be the equilibrium phase for $\text{Na}_{0.67}\text{CoO}_2$ at low temperatures. However, the experimentally observed behaviour is different. Figure 1b summarizes the ex situ experimental synthesis results for the different Na_xCoO_2 polytypes³¹. At low Na content ($0.6 < x < 0.75$), P2 is only synthesized above $\sim 700^\circ\text{C}$ ($\sim 1,000\text{ K}$), while P3 and O3' are obtained at lower temperatures. Thus, the metastable three-layer polytypes are the actually observed low-temperature phases, while the two-layer P2 phase can only be synthesized at high temperature, in apparent contradiction to the DFT stability predictions.

Motivated by the need to understand what drives solid-state reactions in polytypic Na_xMO_2 systems, we undertake an in-depth study of the synthesis of Na_xCoO_2 and Na_xMnO_2 . Using in situ synchrotron XRD and differential scanning calorimetry (DSC), we observe a sequence of non-equilibrium three-layer phases during the solid-state ceramic synthesis of P2-layered sodium metal oxides. We rationalize our findings using an ab initio thermodynamic framework based on a powder precursor interfacial reaction model, and suggest a unifying principle that governs the initial phase formation in solid-state synthesis. Our work elucidates the subtle competition between thermodynamics and kinetics, providing fundamental insights towards a more rational understanding of solid-state ceramic materials synthesis.

In situ experimental study of P2- Na_xCoO_2 synthesis

High-energy synchrotron XRD is a powerful tool to monitor the structural changes and phase evolution during inorganic materials synthesis^{13–17}. To understand the formation of P2- Na_xCoO_2 , we use in situ synchrotron XRD, observing the evolution of different phases from the mixture of precursors to the final compound, varying precursors, heating rate and annealing temperature, as described in the Methods and Supplementary Information.

Figure 2 shows the result of a typical synthesis experiment: the formation of $\text{Na}_{\approx 0.7}\text{CoO}_2$ from a ball-milled mixture of $\text{CoO} + 0.35\text{ Na}_2\text{O}_2$, with a fast heating rate ($36^\circ\text{C min}^{-1}$) up to 850°C in air. Only CoO is observed in the initial XRD scan, as Na_2O_2 amorphizes during ball-milling. The O3 phase with composition NaCoO_2 forms rapidly at 364°C (637 K), about 7 min after the beginning of the synthesis (which starts at $\approx 100^\circ\text{C}$). Figure 2b shows that, despite having a precursor ratio designed to target a $\text{Na}_{0.7}\text{CoO}_2$ stoichiometry, nearly all of the Na reacts with Co in a 1:1 ratio, represented by the reaction:



The reaction is extremely fast—it is complete in one scan ($\approx 75\text{ s}$)—and yields a crystalline O3- NaCoO_2 at nearly full sodiation ($x=0.95(1)$, where the number in brackets indicates the standard deviation on the last significant digit). The rapid phase formation suggests fast oxygen uptake and diffusion of Na cations into the rock salt-type CoO framework, supported by rapid reorganization of the Co cations into layers³². Over the next 15 min (temperature $T=665^\circ\text{C}$ ($\approx 940\text{ K}$)), the evolution of the interlayer spacing and Na occupancy shows that the Na fraction in O3- Na_xCoO_2 decreases from 0.95 to approximately 0.8 (Fig. 2c), after which a new monoclinic O3' phase with $\text{Na}_{0.65(3)}\text{CoO}_2$ composition appears. This change in Na_xCoO_2 stoichiometry results from a reaction between the residual CoO precursor with O3- NaCoO_2 as the system evolves towards the target composition. The O3 \rightarrow O3' transition takes $\approx 6\text{ min}$, after which O3' undergoes a rapid transition ($< 75\text{ s}$) to a P3 phase with large interlayer spacing (5.55 \AA) and low Na content ($0.61(2)$). We speculate that the low Na content in the P3 phase indicates that some sodium may segregate from the layered oxide during the O3' \rightarrow P3 phase transformation, probably as Na_2O . As P3 forms, the amount of CoO decreases rapidly. Interestingly, this O3–O3'–P3 phase transformation sequence observed upon heating is similar to the phase evolution when an O3 oxide is desodiated electrochemically.³³

Finally, when the temperature is maintained constant at 850°C ($\approx 1,123\text{ K}$), P3 transforms into P2- $\text{Na}_{0.67(2)}\text{CoO}_2$. Even though this is the highest temperature, the transition is the slowest: only 14.5(5)% of P2 has formed after 160 min. For this reason, we increased T to 950°C and then $1,050^\circ\text{C}$, and finally obtained a single-phase P2 compound. As evidenced also by its smaller interlayer spacing, P2 accommodates a larger Na content than P3, confirming that the formerly segregated Na is still available in the mixture.

In the Supplementary Information, we discuss hydroxide precursors (Supplementary Fig. 1) and we report complementary

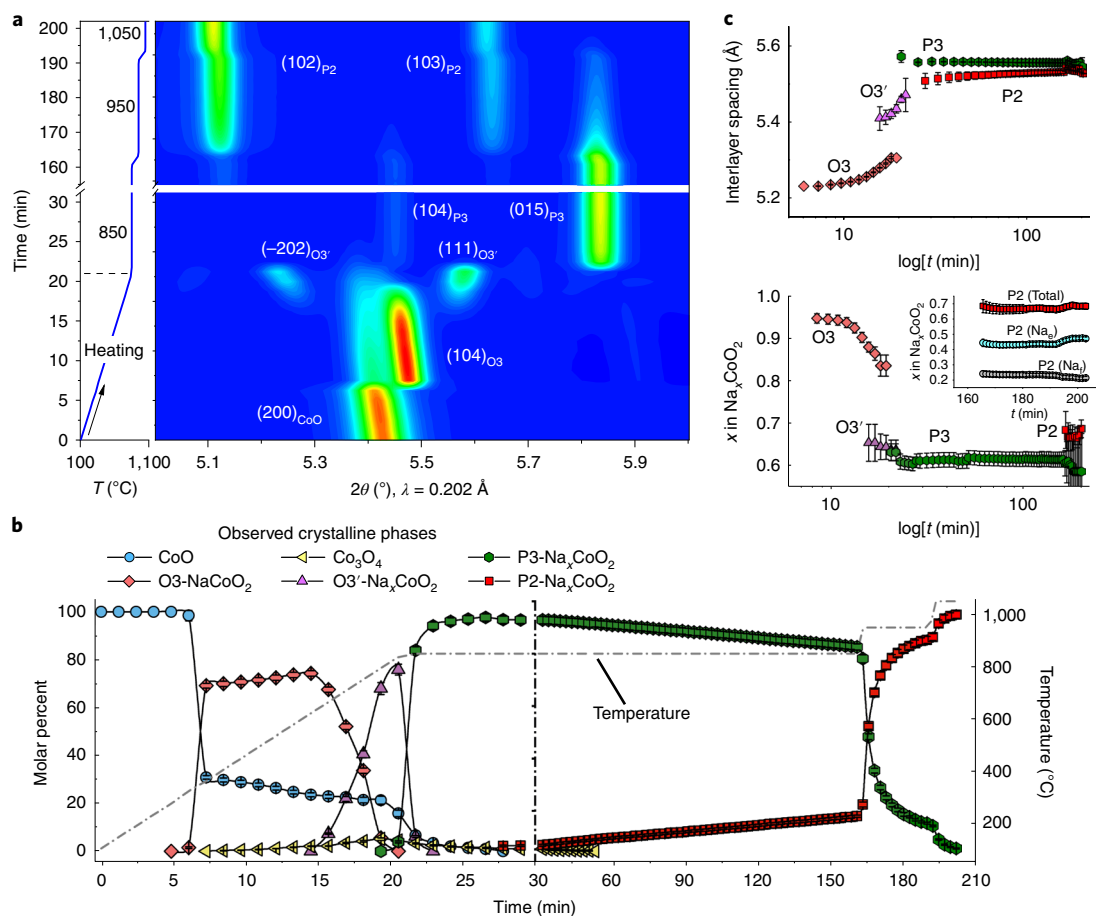


Fig. 2 | Solid-state synthesis of P2-Na_{0.7}CoO₂ monitored by in situ synchrotron XRD. a, Contour plot highlighting the evolution of the Bragg peaks. A sequence of layered compounds is observed (O3 → O3' → P3 → P2). **b, c**, Parameters obtained from Rietveld refinement of the XRD patterns: evolution of the molar percent of the observed crystalline phases (**b**) and interlayer spacing and Na content of each Na_xCoO₂ polytype (**c**). The Na site that is edge-sharing (face-sharing) with the adjacent CoO₆ octahedra is denoted as Na_e(Na_i).

in situ experiments from CoO, showing that annealing at 550 °C results in a similar series of transformations, but without the formation of P2 (Supplementary Fig. 2). Moreover, the heating rate or choice of Co₃O₄ as precursor does not substantially influence the results of the experiment (Supplementary Figs. 2–5), proving that, in the Na_xCoO₂ system, this pathway is robust to synthesis variations. We show later in the section ‘Validation in the Na_xMnO₂ system and effect of precursors’ that this is not the case when a Na₂CO₃ precursor is used.

According to the DFT stability calculations on Na_xCoO₂ in Fig. 1a, P2-Na_{0.67}CoO₂ is the equilibrium phase at low temperature. To confirm that the observed P3 to P2 transition is indeed an irreversible transformation from a metastable to a stable phase, as opposed to a reversible temperature-driven first-order phase transition, we performed DSC on a sample of P3'-Na_{0.67}CoO₂. Figure 3a shows that upon heating an exothermic peak is observed at ≈624 °C and no transition is present upon cooling. After the measurement, we verified by XRD that the P3' sample had become P2, indicating that P2 is indeed lower in energy than P3' and confirming the DFT stability calculations. Furthermore, we confirm that P2 obtained from P3' via annealing at 750 °C never reverts back to the initial P3' structure upon annealing for long times at lower temperatures (Supplementary Fig. 6). Finally, the phase fraction evolution during the P3 to P2 transition follows a characteristic S-shaped profile for which the transformation rate is slow at both the beginning and the end, but rapid in the middle of the reaction. This profile can

be explained and fitted by a nucleation-growth-saturation model, which is qualitatively expressed by an Avrami equation (Fig. 3b)³⁴. The Avrami-like behaviour, together with our DSC results, confirm that P3 → P2 is an exothermic, irreversible phase transformation driven by crystallization kinetics.

Rationalizing the phase evolution of Na_xCoO₂

The observed multistage phase evolution in Fig. 2 can be classified into two major reaction sequences. First, there are a series of fast transformations that occur within 30 min, which proceed through the non-equilibrium three-layer phases O3–O3'–P3 with decreasing Na concentration from O3-Na_{0.95}CoO₂ to P3-Na_{0.61}CoO₂. Second, we observe a slow polymorphic transformation from the metastable P3 phase to the target equilibrium P2 polytype, which proceeds over the next 150 min.

To understand the thermodynamic evolution of the system, we plot the grand-canonical free energy of the entire reaction vessel as a function of time, as shown in Fig. 4a, accounting for open boundary conditions with respect to oxygen as controlled by its chemical potential μ_{O₂} (Methods). The energy cascade shows that nearly all of the reaction free energy is consumed within the first 30 min of the solid-state reaction. Notably, ≈85% of the available reaction energy is consumed 6 min into the reaction to form O3-NaCoO₂. The transformations from O3 to O3' and then P3 consume much of the remaining reaction energy, leaving <2% of the total reaction energy for the polymorphic transformation from P3 to P2.

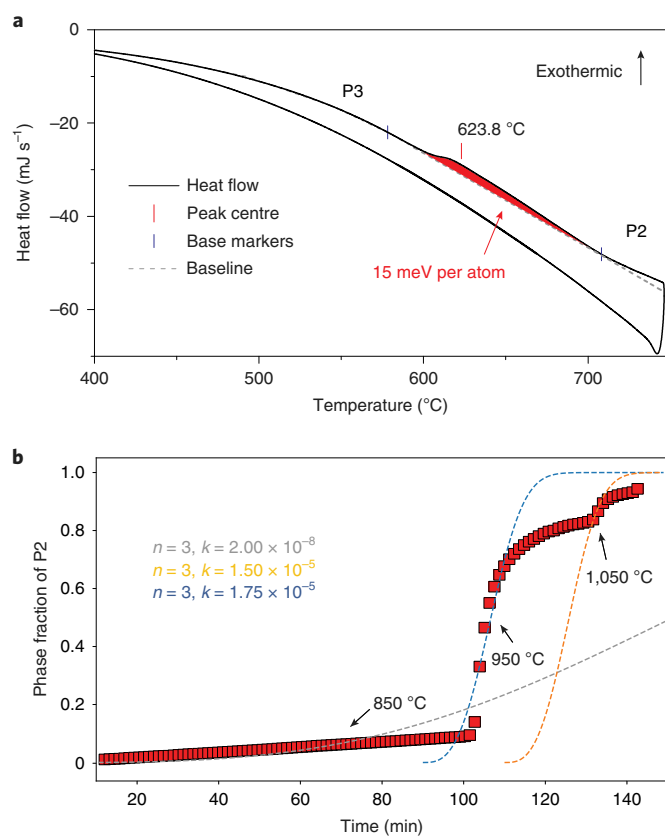


Fig. 3 | P3 to P2 phase transition. **a**, DSC curve of pure P3'- $\text{Na}_{0.67}\text{CoO}_2$ powder (12.67 mg). An exothermic peak is observed at $\approx 624^\circ\text{C}$. The amount of heat released in this phase transition is calculated by integrating the shaded area. **b**, Phase fraction versus time during the P3 to P2 transition obtained from Rietveld refinement and the corresponding fitting by the Avrami equation for three temperature ranges (850, 950 and $1,050^\circ\text{C}$) independently. Note that P3 ($\text{Na}_{0.61}\text{CoO}_2$) to P2 ($\text{Na}_{0.67}\text{CoO}_2$) is not a constant-composition phase transition: it is limited not only by reaction kinetics but also by Na diffusion, which can explain the deviation from perfect Avrami fitting near the end of the transition.

Our energy cascade rationalizes the observed reaction sequence. The fast transformations that occur in the first 30 min are thermodynamically driven by large reaction driving forces. The highest energy reaction is in the formation of O3'- NaCoO_2 , which then transforms to the non-equilibrium O3' and P3 phases. It is well known that displacive transformations are facile between the three-layer polytypes; O3' is a monoclinic distortion of O3- NaCoO_2 associated with Na removal, and P3 can be formed from O3 by sliding the oxygen layer across the Na layer by $(1/3, 1/3, 0)^{22,31,33}$. On the other hand, deriving the P2 phase from O3/P3 requires sliding of the oxygen layer across the Co layer, which has too large an energy barrier to occur by a diffusionless transformation (Supplementary Figs. 7 and 8), meaning the transformation probably proceeds by P2-nucleation instead. However, after 30 min, there is so little thermodynamic driving force remaining that higher temperatures are needed to accelerate the Johnson-Mehl-Avrami-Kolmogorov (JMAK) kinetics of the P3→P2 polymorphic transformation.

Despite preparing a Na:Co precursor ratio to target the $\text{Na}_{0.7}\text{CoO}_2$ composition, the first phase to form is O3- NaCoO_2 , which seems to determine the reaction path by setting the system up for the kinetically facile topotactic transformations through the metastable O3' and P3 three-layer phases. Thus, rationalizing the initial formation

of the O3 phase is crucial to understanding the phase evolution in this system.

What is the mechanism driving this initial O3- NaCoO_2 phase selection? We can achieve some insight into this question by considering that reactions between precursors initiate at the interfaces between powder precursors (Fig. 4). While $\text{Na}_{0.7}\text{CoO}_2$ is the composition of the entire reaction vessel, locally powder precursors of Na_2O_2 and CoO have no knowledge of the total stoichiometric composition of the system. Under these local interfacial boundary conditions, the first nucleus to form has, in principle, a compositionally unconstrained reservoir of Na and Co to form from, for a given applied μ_{O_2} . We demonstrate here that the first phase to form at this interface is the phase with the maximum reaction energy from the precursors. The stoichiometry of this reaction product is compositionally unconstrained; in other words, this maximum reaction energy compound could have any Na/Co ratio—regardless of the prepared precursor ratio. When oxygen transport is fast, the oxygen stoichiometry of the product will be set by the μ_{O_2} of the reaction atmosphere—that is, reducing at high temperatures and low p_{O_2} , and oxidizing at low temperatures and high p_{O_2} .

The reaction energies for various Na_xCoO_2 phases to form at the $\text{CoO}|\text{Na}_2\text{O}_2$ interface in air are shown in Fig. 5, calculated from a thermodynamic grand potential open to an external oxygen reservoir^{1,35}, using a methodology as described in Richards et al.³⁶. The temperature dependence of the free energy is dominated by the entropy of gaseous O_2 , and is approximated without consideration of the entropy in the solids (Methods), meaning that the temperature scale in Fig. 5 and related figures provides a measure of the oxidation potential in the reaction atmosphere. Figure 5a shows that, at all temperatures, the NaCoO_2 composition has the most negative reaction energy of all layered Na_xCoO_2 compositions at the $\text{Na}_2\text{O}_2|\text{CoO}$ interface, and is therefore the composition with the strongest driving force to form. The crucial observation is that the structure selection of the first phase to form is largely governed by composition selection of the maximum compositionally unconstrained reaction energy. Specifically, the NaCoO_2 composition has the largest negative reaction energy under open-system boundary conditions, and the O3 polytype is the ground-state structure for the NaCoO_2 composition (Supplementary Table 1, Fig. 1 and Supplementary Fig. 9).

Since the precursors were prepared at a $\text{Na}_{0.67}\text{CoO}_2$ composition, the initial formation of O3- NaCoO_2 at $\approx 600\text{K}$ leaves the remaining CoO precursor in the reaction vessel (Fig. 2b). The nucleation of P2- $\text{Na}_{0.67}\text{CoO}_2$ around 30 min can further be rationalized by computing the compositionally unconstrained μ_{O_2} -dependent reaction energy between CoO and O3- NaCoO_2 . As shown in Fig. 5b, the reducing conditions at high temperature make it increasingly difficult to stabilize layered oxides of low Na content, whereas at lower temperature they become favourable. Indeed, we find that O3' and P3 are already observed experimentally below 550°C (Supplementary Figs. 2 and 3). At the $\text{CoO}|\text{O3-}\text{NaCoO}_2$ interface above 900 K (Fig. 5b), the most favourable composition to form is $\text{Na}_{0.67}\text{CoO}_2$. However, while the lowest energy structure at the $\text{Na}_{0.67}\text{CoO}_2$ composition is P2 (Supplementary Table 1), the computed P2/P3 energy difference is small (1 meV per atom) so that the reaction sequences O3→O3'→P3 and O3→O3'→P2 are both thermodynamically competitive. The fact that the P3 intermediate is observed experimentally is due to kinetically facile layer shifting from O3' to P3, as opposed to O3' to P2. Our results show that when thermodynamic driving forces are small, kinetically viable structural transformations guide structure selection along the phase transformation pathway⁸. The nucleation of the P2 polytype probably also occurs at low temperature (near 27 min, Fig. 2), providing the germ nuclei for the Avrami reaction in the slow polymorphic transformation regime, but such nuclei can only grow at a measurable rate at high temperature.

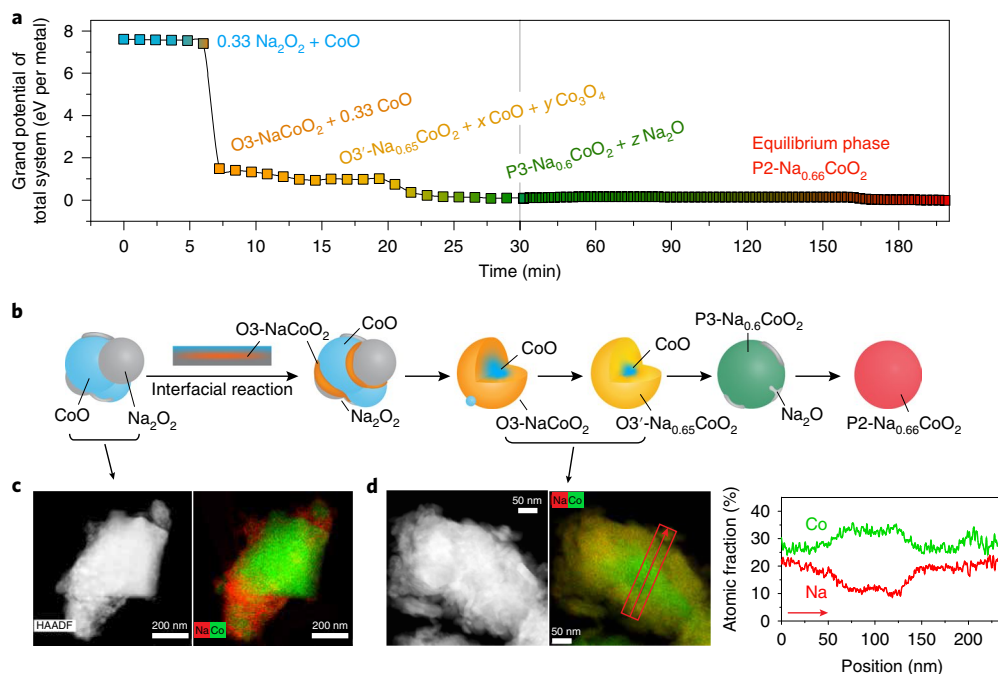


Fig. 4 | Energy cascade and physical model for the solid-state reaction of CoO and Na_2O_2 to form $\text{P}2\text{-Na}_{2/3}\text{CoO}_2$. **a**, Evolution of the grand potential open to an external oxygen reservoir, for the total system in the reaction vessel, normalized by the number of metal cations (Na, Co). Two different scales are used on the time axis to highlight the multiple phase transitions in the first 30 min (same as Fig. 2b). **b**, Cartoon suggesting a physical model of the reaction pathway via interfacial reactions. **c,d**, HAADF-STEM and EDX images showing the pristine $\text{CoO} + 0.35\text{Na}_2\text{O}_2$ powders mixture (**c**), and the same mixture recovered after a brief annealing at 400°C for 90 min (**d**). The HAADF-STEM and EDX images show an imperfect core-shell reaction, with sodiation proceeding inwards from the cobalt oxide particle surface.

It should be noted that the ‘imperfect core-shell’ reactions that we observed in the sequence (Fig. 4) may occur in parallel in certain situations; when spatial parameters (particle size and geometry) limit mass transport one is likely to experimentally observe different reaction progression in different parts of a sample. Studying synthesis pathways should therefore be performed with small-sized and well-mixed precursors to provide results that can be most easily interpreted, as long as the initial reaction can be captured by the time resolution of the experimental characterization techniques.

Conducting similar experiments and reaction analyses using a Co_3O_4 precursor (Supplementary Figs. 4 and 5) leads to similar conclusions (Supplementary Fig. 10). Similar to the CoO case, our calculations illustrate that the initial formation of O3 is driven by the fact that it has the most negative compositionally unconstrained reaction energy (Supplementary Fig. 10a). Then, at the $\text{Co}_3\text{O}_4|\text{O}3\text{-NaCoO}_2$ interface (Supplementary Fig. 10b), the $\text{Na}_{0.67}\text{CoO}_2$ composition can be reached at sufficiently oxidizing conditions, such as low temperatures close to 600 K.

Validation in the Na_xMnO_2 system and effect of precursors

To validate our hypothesis that the first phase to form at powder precursor interfaces is the compound with the maximum compositionally unconstrained reaction energy, we conduct analogous in situ experiments in the Na_xMnO_2 system, using both Na_2O_2 and Na_2CO_3 as precursors. This has particular relevance considering that different synthesis outcomes are obtained when using Na_2CO_3 versus Na_2O_2 in several other Na-layered oxides including $\alpha\text{-NaFeO}_2$ (ref. 37) and $\text{NaNi}_x\text{Mn}_{1-x}\text{O}_2$ (ref. 38). Figure 6 shows the observed phase evolution and reaction energetics for Na_xMnO_2 using Mn_2O_3 and either Na_2O_2 (Fig. 6a–c) or Na_2CO_3 (Fig. 6d,e). When Na_2O_2 is used, the fully sodiated phase $\text{O}3'\text{-NaMnO}_2$ is observed first (Fig. 6a), before it quickly transforms into a Na-deficient P3 phase, similar to the phase evolution in the Na_xCoO_2 system. Figure 6b shows that the

initial $\text{O}3'\text{-NaMnO}_2$ phase has the maximum reaction energy in the $\text{Na}_2\text{O}_2|\text{Mn}_2\text{O}_3$ compositionally unconstrained reaction, which is consistent with the principle we derived for the Co system.

The subsequent formation of $\text{P}3\text{-Na}_{0.42(1)}\text{MnO}_2$, ultimately transforming into P2, is consistent with the predicted Na content at which the unconstrained reaction energy between NaMnO_2 and excess Mn_2O_3 is maximal, as shown in Fig. 6c. Interestingly, after the formation of P3, $\text{O}3'$ forms again and coexists with P2 (Supplementary Fig. 12). This behaviour is the result of the influence of μ_{O_2} on the $\text{O}3'\text{-P}3$ equilibrium and can be well explained by our reaction energy calculations (Supplementary Fig. 13). In short, initially μ_{O_2} is high (low temperature) and P3 is the favourable product. When temperature increases sufficiently (low μ_{O_2}) the situation is reversed and $\text{O}3'$ may form again. This can only occur if a sufficient amount of Na is available, which is the case for Na_xMnO_2 because the formed P3 phase is found to have a lower Na content ($x=0.42$) than P3 in the Co phase (Supplementary Fig. 14).

Figure 6d shows that Mn_2O_3 reacts differently with Na_2CO_3 than it does with Na_2O_2 . Instead of initially forming $\text{O}3'\text{-NaMnO}_2$, the sodium-deficient P3 phase ($\text{P}3\text{-Na}_{\approx 0.4}\text{MnO}_2$) appears first. As the temperature increases, P3 transforms into a mixture of P2 and a phase with a three-dimensional tunnel structure ($3\text{D}\text{-Na}_{\approx 0.4}\text{MnO}_2$)³⁹. Figure 6e shows the reaction energies between Mn_2O_3 and Na_2CO_3 . Unlike the case when Na_2O_2 is the precursor, the sodium-deficient phase $\text{P}3\text{-Na}_{0.33}\text{MnO}_2$ now has the most negative formation energy at intermediate temperatures (for example, $T=600\text{ K}$), which is consistent with the idea that it will first form in the compositionally unconstrained interfacial reaction between the precursors.

Because Na_2CO_3 and Na_2O_2 induce a different reaction path for the Mn system, we also evaluated in situ the synthesis of $\text{Na}_{0.67}\text{CoO}_2$ starting from CoO and Na_2CO_3 (Supplementary Fig. 15). We find that Na_2CO_3 is poorly reactive at low temperature, and thus CoO first oxidizes fully to Co_3O_4 , which then sodiates at higher

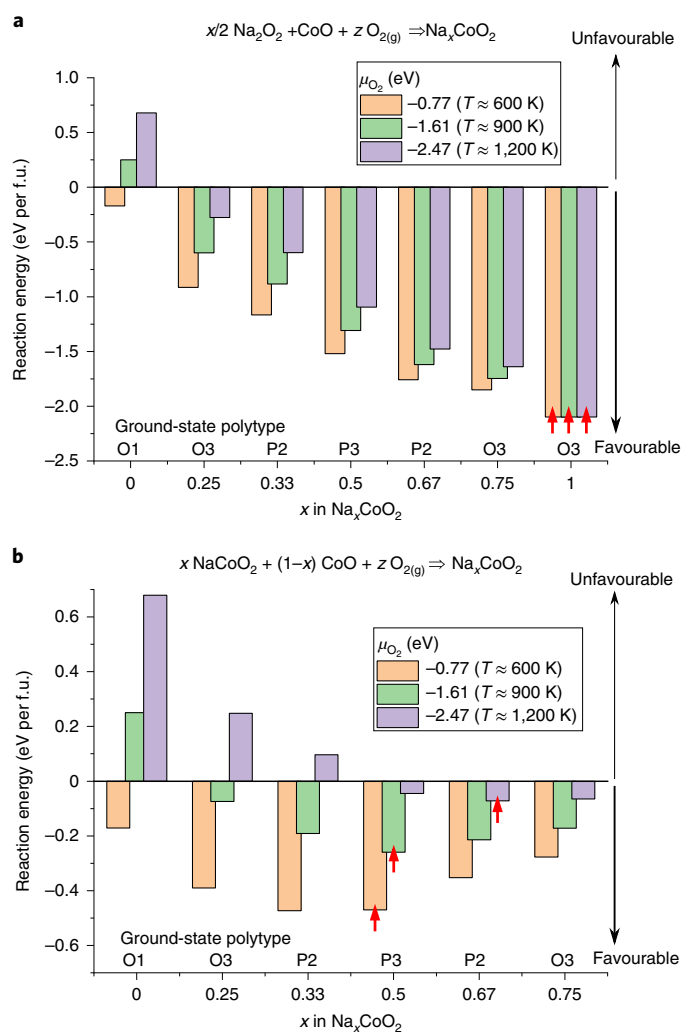


Fig. 5 | Reaction energies for the formation of the lowest-energy Na_xCoO_2 polytype as a function of x . **a**, Reaction energy per formula unit (eV per f.u.) of reaction (1) $x/2 \text{Na}_2\text{O}_2 + \text{CoO} + z\text{O}_{2(g)} \rightarrow \text{Na}_x\text{CoO}_2$. **b**, Reaction energy of reaction (2) $x\text{NaCoO}_2 + (1-x) \text{CoO} + z\text{O}_{2(g)} \rightarrow \text{Na}_x\text{CoO}_2$. NaCoO_2 and $\text{Na}_{0.75}\text{CoO}_2$ are O3-type structures, while $\text{Na}_{0.67}\text{CoO}_2$ is P2 type. The temperatures indicated in the legend correspond to $p_{\text{O}_2} = 1$ atm and are approximate (Methods). Red arrows indicate the most negative reaction energy bars, for each given μ_{O_2} .

temperature. Interestingly, the first phase to form is not O3- NaCoO_2 ; a P3 polymorph forms first, followed by P2. We calculate new reaction energies for the $\text{Na}_2\text{CO}_3|\text{Co}_3\text{O}_4$ interface (Supplementary Fig. 16), which yields a prediction of the P3 polymorph as the compositionally unconstrained maximum reaction energy product, consistent with our experimental observation.

In conclusion, despite the short in situ reaction times (<1 h), we are able to capture the first phase to form, and we validate the theory that the compound with the most negative compositionally unconstrained reaction energy governs the composition and structure of the first phase to form. Additionally, our theory can rationalize how changing precursors influences this first phase. Different Na precursors (Na_2O_2 versus Na_2CO_3) exhibit different Na chemical potentials, which in turn create a different dependence of the reaction free energy as a function of x in Na_xMO_2 . In Fig. 6f, we show that the higher the Na chemical potential in the precursor, the more the reaction free energies will tilt favourably towards compounds with high Na content. For the precursors with ‘loosely bound’ sodium with high μ_{Na}

(Na_2O , -2.06 eV; Na_2O_2 , -2.379 eV), a fully sodiated O3 phase has the most negative formation energy, whereas when Na is ‘locked up’ in the stable Na_2CO_3 phase ($\mu_{\text{Na}} = -3.69$ eV) the trend is reversed, resulting in the preferable formation of sodium-deficient phases.

Conclusion

Understanding the role of thermodynamics versus kinetics during materials formation is a foundational question in materials processing and synthesis science. Although qualitative heuristics for navigating these concepts are commonplace, it has been difficult to establish a quantitatively rigorous understanding of the competition between thermodynamics and kinetics for real synthesis reactions. This has been due to two reasons: (1) reactions occur in a ‘black box’, meaning that the initial phase evolution often remains unknown; (2) the energies of these reactions are difficult to measure as a function of reaction progress.

In this work, we leveraged in situ synchrotron XRD to characterize the early stages of phase evolution for Na_xCoO_2 and Na_xMnO_2 during solid-state ceramic synthesis. In contrast to the traditional belief that solid-state reactions are slow, we observed a number of fast reactions that take place within minutes of initiating synthesis. By combining the observed reaction pathways with ab initio thermodynamics, we were able to show that the first phase to form can consume the majority of the total reaction free energy and topotactically template the structural evolution through a series of non-equilibrium phases. To rationalize the structure-selection mechanism of the first phase to form, we proposed a model where the first phase to nucleate at the interface between solid-state powder precursors is the compound, or set of compounds, with the maximum compositionally unconstrained reaction energy. This first phase to form has the composition with the most negative reaction free energy, and its structure is governed by the ground-state crystal structure at such a composition. We note that this mechanism is particularly relevant in reactions where thermodynamic driving forces are large, such as solid-state chemical reactions. In synthesis methods at lower temperatures and with smaller driving forces (of the order of $k_{\text{B}}T$, where k_{B} is the Boltzmann constant), such as hydrothermal synthesis, structure selection may instead be driven by size-dependent thermodynamics and competitive nucleation kinetics^{16,40–43}.

The compositionally unconstrained powder reaction model has two major consequences: (1) the first phase to form does not necessarily have the composition corresponding to the overall precursor composition in the reaction vessel; and (2) the first phase to form can be targeted by careful precursor selection, as demonstrated by switching from Na_2O_2 to Na_2CO_3 in both Co and Mn systems. This rationalization of the first phase to form creates a valuable design handle by which reaction paths can be tailored to go through, or circumvent, specific non-equilibrium intermediates.

While we often separate thermodynamics and kinetics conceptually, our analysis here shows that they are intimately coupled during the early stages of materials formation. Fast reaction kinetics during multistage crystallization are a consequence of large thermodynamic driving forces, whereas small driving forces lead to slow kinetics, requiring high reaction temperatures for reactions to complete, as demonstrated by the formation conditions of the P2 phase in this work. We argue that the high reaction energy from the precursors will thermodynamically govern the composition and structure of the first phase to form, while the ensuing transformations can often be kinetically selected by simple compositional variations, or by topotactically facile layer shifting, as is the case in the layered compounds that we have studied. By better understanding the intricate relationship between thermodynamics and kinetics during materials formation, this work facilitates the design of more sophisticated strategies towards the targeted synthesis of inorganic materials.

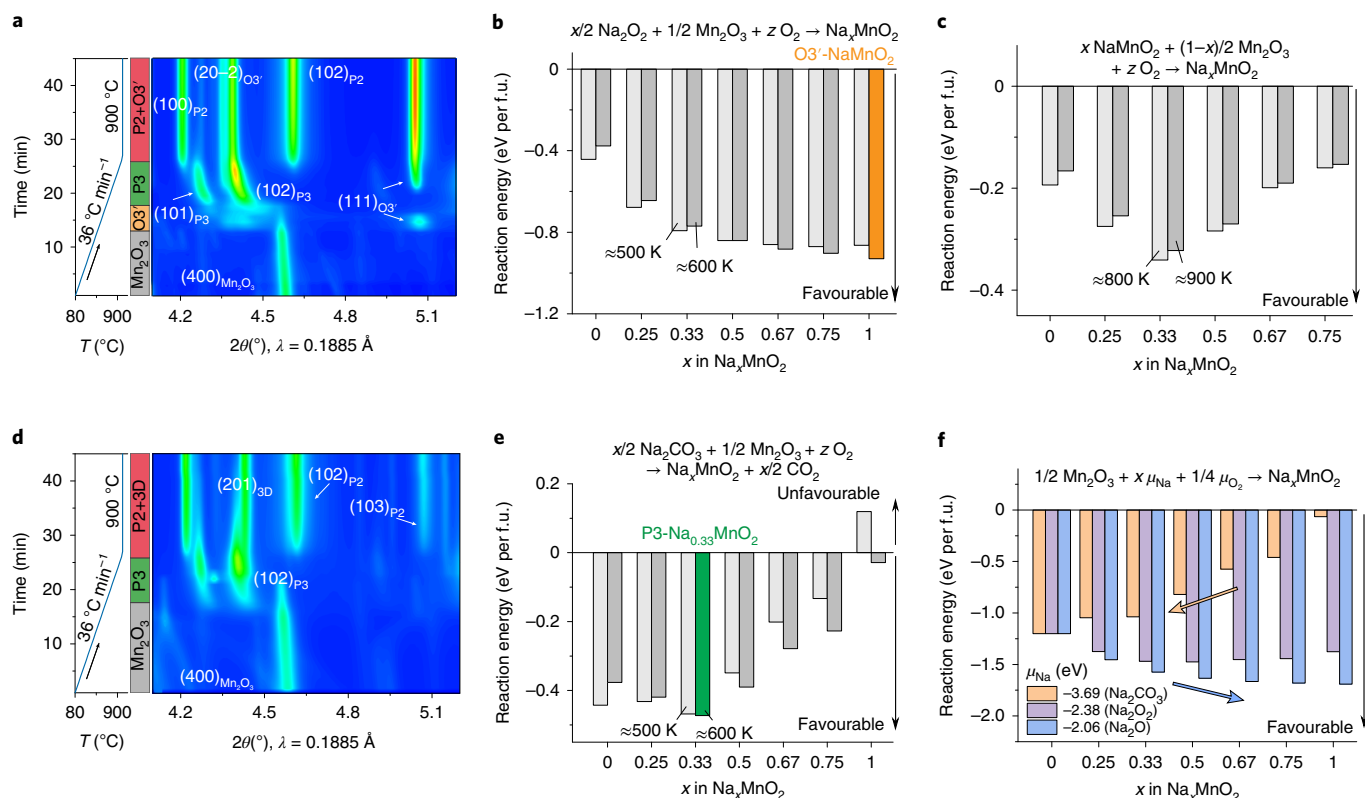


Fig. 6 | Generalization to the Na_xMnO_2 system of in situ XRD during solid-state synthesis and reaction energy calculations. **a**, In situ XRD pattern of the reaction between $1/2 \text{Mn}_2\text{O}_3 + 1/3 \text{Na}_2\text{O}_2$. Note that NaMnO_2 is labelled as $\text{O}3'$ because the Jahn-Teller active Mn^{3+} induces a monoclinic distortion. The final P2 is a pure hexagonal phase at $1,050^\circ\text{C}$, while after cooling it yields a mixture of hexagonal P2 (with Mn vacancies) and distorted orthorhombic P2' (Supplementary Fig. 11), in agreement with the literature^{46,47}. **b**, Reaction energies between Mn_2O_3 and Na_2O_2 , according to the reaction $x/2 \text{Na}_2\text{O}_2 + 1/2 \text{Mn}_2\text{O}_3 + z\text{O}_2 \rightarrow \text{Na}_x\text{MnO}_2$. $\text{O}3'$ - NaMnO_2 has the most negative formation energy at the beginning of the synthesis ($\approx 600\text{K}$, orange bar). **c**, Reaction energies between Mn_2O_3 and $\text{O}3'$ - NaMnO_2 , according to the reaction $x\text{NaMnO}_2 + (1-x)/2 \text{Mn}_2\text{O}_3 + z\text{O}_2 \rightarrow \text{Na}_x\text{MnO}_2$. **d**, In situ XRD pattern of the reaction between $1/2 \text{Mn}_2\text{O}_3 + 1/3 \text{Na}_2\text{CO}_3$. **e**, Reaction energies between Mn_2O_3 and Na_2CO_3 , according to the reaction $x/2 \text{Na}_2\text{CO}_3 + 1/2 \text{Mn}_2\text{O}_3 + z\text{O}_2 \rightarrow \text{Na}_x\text{MnO}_2 + x/2 \text{CO}_2$. $\text{P}3$ - $\text{Na}_{0.33}\text{MnO}_2$ has the most negative formation energy at the beginning of the synthesis ($\approx 600\text{K}$, green bar). **f**, Reaction energies between Mn_2O_3 and various Na precursors at fixed μ_{O_2} (0 eV) according to $1/2 \text{Mn}_2\text{O}_3 + x\mu_{\text{Na}} + 1/4 \mu_{\text{O}_2} \rightarrow \text{Na}_x\text{MnO}_2$. The temperatures in **b**, **c** and **e** are approximate (Methods).

Online content

Any methods, additional references, Nature Research reporting summaries, source data, extended data, supplementary information, acknowledgements, peer review information; details of author contributions and competing interests; and statements of data and code availability are available at <https://doi.org/10.1038/s41563-020-0688-6>.

Received: 1 September 2019; Accepted: 19 April 2020;

Published online: 18 May 2020

References

- Ong, S. P., Wang, L., Kang, B. & Ceder, G. Li-Fe-P-O-2 phase diagram from first principles calculations. *Chem. Mater.* **20**, 1798–1807 (2008).
- Andersson, J. O., Helander, T., Hoglund, L. H., Shi, P. F. & Sundman, B. THERMO-CALC & DICTRA, computational tools for materials science. *Thermochemistry* **26**, 273–312 (2002).
- Bianchini, M., Wang, J., Clément, R. & Ceder, G. A first-principles and experimental investigation of nickel solubility into the P2 Na_xCoO_2 sodium-ion cathode. *Adv. Energy Mater.* **8**, 1801446 (2018).
- Narayan, A. et al. Computational and experimental investigation for new transition metal selenides and sulfides: the importance of experimental verification for stability. *Phys. Rev. B* **94**, 045105 (2016).
- Sun, W. et al. The thermodynamic scale of inorganic crystalline metastability. *Sci. Adv.* **2**, e1600225 (2016).
- Aykol, M., Dwaraknath, S. S., Sun, W. & Persson, K. A. Thermodynamic limit for synthesis of metastable inorganic materials. *Sci. Adv.* **4**, eaaq0148 (2018).
- Gopalakrishnan, J. Chimie douce approaches to the synthesis of metastable oxide materials. *Chem. Mater.* **7**, 1265–1275 (1995).
- Stein, A., Keller, S. W. & Mallouk, T. E. Turning down the heat – design and mechanism in solid-state synthesis. *Science* **259**, 1558–1564 (1993).
- Chen, Y., Rangasamy, E., dela Cruz, C. R., Liang, C. & An, K. A study of suppressed formation of low-conductivity phases in doped $\text{Li}_x\text{La}_3\text{Zr}_2\text{O}_{12}$ garnets by in situ neutron diffraction. *J. Mater. Chem. A* **3**, 22868–22876 (2015).
- Wang, L. et al. Structure tracking aided design and synthesis of $\text{Li}_3\text{V}_2(\text{PO}_4)_3$ nanocrystals as high-power cathodes for lithium ion batteries. *Chem. Mater.* **27**, 5712–5718 (2015).
- Eriksson, R. et al. Formation of tavorite-type LiFeSO_4F followed by in situ X-ray diffraction. *J. Power Sources* **298**, 363–368 (2015).
- Jensen, K. M. Ø., Tyrsted, C., Bremholm, M. & Iversen, B. B. In situ studies of solvothermal synthesis of energy materials. *ChemSusChem* **7**, 1594–1611 (2014).
- Shoemaker, D. P. et al. In situ studies of a platform for metastable inorganic crystal growth and materials discovery. *Proc. Natl Acad. Sci. USA* **111**, 10922–10927 (2014).
- Jiang, Z., Ramanathan, A. & Shoemaker, D. P. In situ identification of kinetic factors that expedite inorganic crystal formation and discovery. *J. Mater. Chem. C* **5**, 5709–5717 (2017).
- Martinolich, A. J. & Neilson, J. R. Toward reaction-by-design: achieving kinetic control of solid state chemistry with metathesis. *Chem. Mater.* **29**, 479–489 (2017).
- Chen, B.-R. et al. Understanding crystallization pathways leading to manganese oxide polymorph formation. *Nat. Commun.* **9**, 2553 (2018).
- He, H. et al. Combined computational and experimental investigation of the La_2CuO_4 - $x\text{S}_x$ ($0 \leq x \leq 4$) quaternary system. *Proc. Natl Acad. Sci. USA* **115**, 7890–7895 (2018).

18. Kohlmann, H. Looking into the black box of solid-state synthesis. *Eur. J. Inorg. Chem.* **2019**, 4174–4180 (2019).
19. Curtarolo, S. et al. The high-throughput highway to computational materials design. *Nat. Mater.* **12**, 191–201 (2013).
20. Zunger, A. Inverse design in search of materials with target functionalities. *Nat. Rev. Chem.* **2**, 0121 (2018).
21. Jain, A., Shin, Y. & Persson, K. A. Computational predictions of energy materials using density functional theory. *Nat. Rev. Mater.* **1**, 15004 (2016).
22. Braconnier, J. J., Delmas, C., Fouassier, C. & Hagenmuller, P. Electrochemical behavior of the phases Na_xCoO_2 . *Mater. Res. Bull.* **15**, 1797–1804 (1980).
23. Lee, M. et al. Large enhancement of the thermopower in Na_xCoO_2 at high Na doping. *Nat. Mater.* **5**, 537–540 (2006).
24. Takada, K. et al. Superconductivity in two-dimensional CoO_2 layers. *Nature* **422**, 53–55 (2003).
25. Delmas, C., Fouassier, C. & Hagenmuller, P. Structural classification and properties of the layered oxides. *Phys. B+C.* **99**, 81–85 (1980).
26. Delmas, C., Fouassier, C. & Hagenmuller, P. Relative stability of octahedral and trigonal prismatic coordination in layered alkaline oxides A_xMO_2 (x less than or equal to 1). *Mater. Res. Bull.* **11**, 1483–1488 (1976).
27. Parant, J. P., Olazcuaga, R., Devalette, M., Fouassier, C. & Hagenmuller, P. Sur quelques nouvelles phases de formule Na_xMnO_2 (x 1). *J. Solid State Chem.* **3**, 1–11 (1971).
28. Yabuuchi, N., Kubota, K., Dahbi, M. & Komaba, S. Research development on sodium-ion batteries. *Chem. Rev.* **114**, 11636–11682 (2014).
29. Mo, Y., Ong, S. P. & Ceder, G. Insights into diffusion mechanisms in P2 layered oxide materials by first-principles calculations. *Chem. Mater.* **26**, 5208–5214 (2014).
30. Guo, S. et al. Understanding sodium-ion diffusion in layered P2 and P3 oxides via experiments and first-principles calculations: a bridge between crystal structure and electrochemical performance. *NPG Asia Mater.* **8**, e266 (2016).
31. Lei, Y. C., Li, X., Liu, L. & Ceder, G. Synthesis and stoichiometry of different layered sodium cobalt oxides. *Chem. Mater.* **26**, 5288–5296 (2014).
32. Bianchini, M., Fauth, F., Hartmann, P., Brezesinky, T. & Janek, J. An in situ structural study on the synthesis and decomposition of LiNiO_2 . *J. Mater. Chem. A* **8**, 1808–1820 (2020).
33. Delmas, C., Braconnier, J.-J., Fouassier, C. & Hagenmuller, P. Electrochemical intercalation of sodium in Na_xCoO_2 bronzes. *Solid State Ion.* **3**, 165–169 (1981).
34. Avrami, M. Kinetics of phase change. I General theory. *J. Chem. Phys.* **7**, 1103–1112 (1939).
35. Wang, L., Maxisch, T. & Ceder, G. A first-principles approach to studying the thermal stability of oxide cathode materials. *Chem. Mater.* **19**, 543–552 (2007).
36. Richards, W. D., Miara, L. J., Wang, Y., Kim, J. C. & Ceder, G. Interface stability in solid-state batteries. *Chem. Mater.* **28**, 266–273 (2016).
37. Takeda, Y., Akagi, J., Edagawa, A., Inagaki, M. & Naka, S. A preparation and polymorphic relations of sodium iron-oxide (NaFeO_2). *Mater. Res. Bull.* **15**, 1167–1172 (1980).
38. Fielden, R. & Obrovac, M. N. Investigation of the $\text{NaNi}_x\text{Mn}_{1-x}\text{O}_{(2)}$ ($0 \leq x \leq 1$) system for Na-ion battery cathode materials. *J. Electrochem. Soc.* **162**, A453–A459 (2015).
39. Akimoto, J. et al. Single-crystal synthesis and structure refinement of $\text{Na}_{0.44}\text{MnO}_2$. *Solid State Phenom.* **170**, 198–202 (2011).
40. Sun, W., Jayaraman, S., Chen, W., Persson, K. A. & Ceder, G. Nucleation of metastable aragonite CaCO_3 in seawater. *Proc. Natl Acad. Sci. USA* **112**, 3199–3204 (2015).
41. Sun, W., Kitchaev, D. A., Kramer, D. & Ceder, G. Non-equilibrium crystallization pathways of manganese oxides in aqueous solution. *Nat. Commun.* **10**, 573 (2019).
42. Navrotsky, A. Nanoscale effects on thermodynamics and phase equilibria in oxide systems. *ChemPhysChem* **12**, 2207–2215 (2011).
43. Ma, X. et al. Guiding synthesis of polymorphs of materials using nanometric phase diagrams. *J. Am. Chem. Soc.* **140**, 17290–17296 (2018).
44. Sun, J., Ruzsinszky, A. & Perdew, J. P. Strongly constrained and appropriately normed semilocal density functional. *Phys. Rev. Lett.* **115**, 036402 (2015).
45. Blangero, M. et al. High-temperature phase transition in the three-layered sodium cobaltite $\text{P}3\text{-Na}_x\text{CoO}_2$ (x similar to 0.62). *Phys. Rev. B* **77**, 18 (2008).
46. Stoyanova, R. et al. Stabilization of over-stoichiometric Mn^{4+} in layered $\text{Na}_{2/3}\text{MnO}_2$. *J. Solid State Chem.* **183**, 1372–1379 (2010).
47. Kumakura, S., Tahara, Y., Kubota, K., Chihara, K. & Komaba, S. Sodium and manganese stoichiometry of P2-type $\text{Na}_{2/3}\text{MnO}_2$. *Angew. Chem. Int. Ed.* **55**, 12760–12763 (2016).

Publisher's note Springer Nature remains neutral with regard to jurisdictional claims in published maps and institutional affiliations.

© The Author(s), under exclusive licence to Springer Nature Limited 2020

Methods

Synthesis and experimental characterization. O3-NaCoO₂ was synthesized using a conventional solid-state method. Stoichiometric amounts of Co₃O₄ (Aldrich, 99.5%, nanopowder) and Na₂O₂ (Aldrich, 97%) were mixed thoroughly by a Spex Mixer/Mill 8000M for 90 min. The precursors were then pressed into pellets before annealing at 450 °C for 16 h under flowing oxygen. P3'-Na_{0.67}CoO₂ was prepared by chemically desodiating O3-NaCoO₂. Stoichiometric amounts of O3-NaCoO₂ and NO₂BF₄ (Aldrich, ≥95%) were added to acetonitrile (Aldrich, 99.8%, anhydrous) in an argon-filled glovebox. NO₂BF₄ dissolves while Na_xCoO₂ remains as a solid phase. The solution was then stirred for 2 d before the resulting black powder was filtered and washed three times with acetonitrile. The sample was then dried at 70 °C in vacuum overnight and stored in the argon-filled glovebox.

The DSC measurements were performed using a SDT Q600 system (TA Instruments). Here 12.67 mg of P3'-Na_{0.67}CoO₂ powder was heated from room temperature to 750 °C at a heating rate of 5 °C min⁻¹ under flowing argon and then cooled at the same rate. The powder after DSC was recovered and used for XRD analysis using a Rigaku diffractometer, in Bragg–Brentano geometry with Cu Kα radiation.

For the in situ synthesis, we target the formation of Na_{0.7}CoO₂ by using different oxide precursors (CoO (Alfa, 99.995%) and Co₃O₄) with Na₂O₂ as sodium source. Two sets of precursors were mixed (Spex Mixer/Mill 8000M for 90 min), pelletized and then annealed at 550 and 850 °C in air, respectively. Two heating rates were used, one fast (36 °C min⁻¹) and one slow (0.5 °C min⁻¹). A synthesis experiment was also carried out using a mixture of CoO and Na₂CO₃. For the in situ synthesis of the Na–Mn–O system, two sets of precursors, 0.67Na₂O₃+Mn₂O₃ and 0.6Na₂CO₃+Mn₂O₃, were mixed (Spex Mixer/Mill 8000M for 90 min), pelletized and then annealed at 900 °C in air, respectively, with a heating rate of (36 °C min⁻¹). In situ synchrotron XRD was performed at F2 (CHESS) and 28-ID-2 (NSLS-II, Brookhaven National Laboratory) for the experiment described in the main text (Fig. 2, CHESS; Fig. 6, BNL). Then 28-ID-2 (NSLS-II, Brookhaven National Laboratory), F2 (CHESS) and 17-BM-B (Advanced Photon Source, Argonne National Laboratory) were used for experiments in the Supplementary Information. Each scan takes ≈12 s and the interval between the end of a scan and the beginning of the next one is 1 or 3 min (varying from experiment to experiment, for data processing). The in situ synthesis experiment using Na₂CO₃ and CoO was performed in a Bruker D8 diffractometer using Bragg–Brentano geometry (starting from 200 °C, a 1-h-long XRD scan was taken every 50 °C).

For transmission electron microscopy (TEM), the powder samples were diluted in hexane and sonicated to obtain good particle dispersion. The TEM samples were prepared by drop casting the solution onto a standard 400 copper mesh TEM grid with lacey carbon support. The samples were loaded into a Gatan 648 vacuum-transfer holder to transfer the sample from the glovebox to the microscope in an inert Ar atmosphere. The high-angle annular dark-field scanning transmission electron microscopy (HAADF-STEM) and energy-dispersive X-ray (EDX) maps were performed on a FEI TitanX 60–300 microscope equipped with a Bruker windowless EDX detector at an acceleration voltage of 200 kV. The particle sizes for the Co and Mn oxides used in our experiments were found to be of a few hundred nanometres (100–400 nm) after ball-milling of the precursor mixture. Na precursors retain instead little crystallinity and have smaller particle size.

Rietveld refinement was carried out using Fullprof⁶⁸. Multiple phases were included in each refinement. A point-by-point background was manually selected. Zero-shift value was refined in the first scan and then kept constant for all subsequent scans. Peak shapes were modelled with a Thompson–Cox–Hastings pseudo-Voigt function. Peak width parameters (*U*, *V*, *W*, *X* and *Y* as defined in Fullprof) were kept as constant as possible between scans, although the subsequent nucleation of different phases induced peak width variation and thus made it necessary to refine them (mostly *X*). Unit cell parameters were always refined for all phases. Fractional atomic coordinates, site occupancy factors and Debye–Waller factors, as a rule of thumb, were refined whenever the relative phase was more than ≈10 wt% to avoid divergence. Debye–Waller factors were refined as a common value for all atoms in a given phase. Refinements were deemed acceptable only when the goodness-of-fit indicator R_{bragg} (as defined in Fullprof) of the main phases was consistently <10.

First-principles calculations. Spin-polarized DFT calculations⁶⁹ were carried out using the Vienna Ab Initio Simulation Package⁵⁰ and the projector-augmented wave method⁵¹. Each calculation used a reciprocal space discretization of 25 Å⁻¹ and consisted of two sequential structural optimization steps, where both lattice parameters and atomic positions were relaxed in the absence of symmetry constraints. The threshold energy difference for self-consistent field convergence in the total free energy was set to 1 × 10⁻³ eV, and a Gaussian-type smearing of the Fermi level was applied. We note that the relative stability of various P2-Na_xCoO₂ configurations obtained using total energy convergence criteria of 1 × 10⁻³ and 1 × 10⁻⁵ eV yielded very similar results, so that the less stringent convergence criterion was deemed sufficient here. A plane wave energy cutoff of 520 eV was used throughout. The choice of the SCAN (strongly constrained and appropriately normed) meta-GGA exchange-correlation functional was motivated by its accurate prediction of the energy and structure of materials with diverse bonding, and its

comparable efficiency to that of standard LDA (local density approximation) and GGA (generalized gradient approximation) functionals^{44,52,53}.

Construction of finite-temperature phase diagrams. To determine the energy above the convex hull of Na_xCoO₂ structures and to construct a ternary Na–Co–O phase diagram (Supplementary Fig. 9), calculations were performed on O₂, CoO, Co₃O₄, Na₂O₂ and Na_xCoO₂ structures (0 ≤ *x* ≤ 1) using analogous parameters to those described above ('First-principles calculations' section). The ground-state Na/vacancy configurations of the various O3, P2 and P3 Na_xCoO₂ (0 < *x* < 1) phases considered in this work were determined in two steps. First, the energies of several hundred possible Na/vacancy orderings at different Na content were computed using the fast GGA+U functional. For all structures with energy below 50 meV per atom from the convex hull (between 60 and 300 Na/vacancy configurations, depending on the Na content) the ground-state configuration was recalculated using the more accurate SCAN meta-GGA functional. For the lowest enthalpy O3, P2 and P3 structures, we calculated vibrational phonon contributions to the free energy⁵⁴, finding that they do not affect the qualitative polymorphic energy orderings from Table 1; details are provided in the Supplementary Information (Supplementary Fig. 17). Finite-temperature phase stability and compositionally unconstrained reaction energies were evaluated by including the entropy of O₂ gas, while assuming Δ*S* (entropy change) between the solid phases to be negligible, as is common for equilibria against oxygen¹. The free energy of O₂(*g*) is obtained as:

$$E_{\text{O}_2} = H_{\text{O}_2} - S_{\text{O}_2} \times T, \quad (1)$$

where H_{O_2} is the 0 K formation enthalpy obtained for an isolated O₂ dimer using SCAN, and S_{O_2} is the experimental entropy at the temperature (*T*) of interest obtained from the JANAF thermochemical tables⁵⁵. Likewise, the free energy of CO₂(*g*) was calculated as:

$$E_{\text{CO}_2} = H_{\text{CO}_2} - S_{\text{CO}_2} \times T. \quad (2)$$

Grand-canonical reaction energy calculations. Reaction energies to form the ground-state Na_xCoO₂ polytypes at various *x* contents were obtained from a grand-canonical ensemble description at different oxygen chemical potentials, μ_{O_2} . As described by Ong et al.¹, μ_{O_2} takes the form:

$$\mu_{\text{O}_2}(T, p_{\text{O}_2}) = h_{\text{O}_2}(T, p_0) - T \left(s_{\text{O}_2}(T, p_0) - k_{\text{B}} \times \ln \left(\frac{p_{\text{O}_2}}{p_0} \right) \right) \quad (3)$$

where p_0 is the reference pressure, p_{O_2} is the O₂ partial pressure and k_{B} is the Boltzmann constant. Lower case h_{O_2} and s_{O_2} denote the enthalpy and entropy of oxygen gas per O₂ molecule. In this work, μ_{O_2} values are referenced such that $\mu_{\text{O}_2} = 0$ eV per O₂ under standard conditions of temperature and pressure ($T = 298.15$ K and $p_{\text{O}_2} = p_0 = 1$ atm). So while the trends we observe are meaningful, as proven in similar recent work³, the exact temperature values may be offset with respect to the experimental ones. Reaction energies are calculated according to the specific reaction equations provided in each figure caption, without further normalization.

The relative chemical potential of Na in a particular Na precursor (for example, Na₂O₂) in Fig. 6f is defined as the difference between the precursor's formation energy and the chemical potential of all other elements in the precursor (in Na₂O₂: $\mu_{\text{Na}} = \frac{1}{2}(\mu_{\text{Na}_2\text{O}_2} - \mu_{\text{O}_2})$). For sodium binary oxides, the free energy of O₂(*g*) at ambient temperature is taken as the reference μ_{O_2} . For Na₂CO₃, the chemical potential of CO₂(*g*) at ambient temperature is taken as reference.

Constructing the energy cascade. The energy cascade is constructed by multiplying the in situ XRD observed phase fraction of each phase at a given time by its grand-canonical free energy, $\phi = G - n_{\text{O}_2}\mu_{\text{O}_2}$, where *G* is the Gibbs free energy of the phase and the μ_{O_2} value is the one discussed above ('Grand-canonical reaction energy calculations' section). The numbers of Na and Co ions are conserved throughout the entire reaction, while oxygen is in exchange with the open air reservoir, so the grand-canonical free energy is normalized to the overall metal concentrations throughout the reaction; Na = 0.67, Co = 1. The Na₂O₂ phase is amorphous (XRD not well suited to its quantification), so we infer its phase fraction in the early stages of synthesis from the concentrations of CoO and NaCoO₂, where we assume that all the Na₂O₂ is consumed in this initial reaction. In the O3' → P3 transformation, the Na concentration in the layered phase decreases from approximately 0.67 to 0.6. We assume that the Na is ejected from the layer phase in an oxide form, whose grand free energy can be approximated by the energy of solid Na₂O. For the energy cascade, $\phi = 0$ eV per metal is set to the grand free energy of P2-Na_{0.67}CoO₂, which is the equilibrium phase at all temperatures throughout the reaction. Formation energies for intermediate *x* in O3-Na_xCoO₂ from 0.8 < *x* < 1.0 are derived from the ordered structures in Kaufman and Van der Ven⁵⁶.

Data availability

All relevant data within the article are available from the corresponding author on request. Source data for the figures are provided with the paper.

References

48. Rodriguez-Carvajal, J. Recent advances in magnetic-structure determination by neutron powder diffraction. *Phys. B* **192**, 55–69 (1993).
49. Hohenberg, P. & Kohn, W. Inhomogeneous electron gas. *Phys. Rev.* **136**, B864–B871 (1964).
50. Kresse, G. & Furthmüller, J. Efficiency of ab-initio total energy calculations for metals and semiconductors using a plane-wave basis set. *Comput. Mater. Sci.* **6**, 15–50 (1996).
51. Blöchl, P. E. Projector augmented-wave method. *Phys. Rev. B* **50**, 17953–17979 (1994).
52. Kitchaev, D. A. et al. Energetics of MnO₂ polymorphs in density functional theory. *Phys. Rev. B* **93**, 045132 (2016).
53. Yang, J. H., Kitchaev, D. A. & Ceder, G. Rationalizing accurate structure prediction in the meta-GGA SCAN functional. *Phys. Rev. B* **100**, 035132 (2019).
54. Togo, A. & Tanaka, I. First principles phonon calculations in materials science. *Scr. Mater.* **108**, 1–5 (2015).
55. Linstrom, P. J. and Mallard, W. G. *NIST Chemistry WebBook* NIST Standard Reference Database Number 69 (NIST, 2018); <https://doi.org/10.18434/T4D303>
56. Kaufman, J. L. & Van der Ven, A. Na₂CoO₂ phase stability and hierarchical orderings in the O3/P3 structure family. *Phys. Rev. Mater.* **3**, 015402 (2019).

Acknowledgements

Funding for this study was provided by the US Department of Energy, Office of Science, Basic Energy Sciences, under contract No. UGA-0-41029-16/ER392000 as a part of the Department of Energy Frontier Research Center for Next Generation of Materials Design: Incorporating Metastability, and supported by the Samsung Advanced Institute of Technology. This work used the 28-ID-2 (XPD) beamline of the National Synchrotron Light Source II (NSLS-II), a US Department of Energy (DOE) Office of Science User Facility operated for the DOE Office of Science by Brookhaven National Laboratory under contract No. DE-SC0012704. Work conducted at the Cornell High Energy

Synchrotron Source (CHESS) is supported by the National Science Foundation under award No. DMR-1332208. Work at the Advanced Photon Source (APS) at Argonne National Laboratory was supported by the US Department of Energy, Office of Science, Office of Basic Energy Sciences under contract No. DE-AC02-06CH11357. The TEM characterizations were performed at the Molecular Foundry, Lawrence Berkeley National Laboratory (LBNL), supported by the Office of Science, Office of Basic Energy Sciences, of the US Department of Energy under contract No. DE-AC02-05CH11231. We acknowledge W. Xu for the assistance at APS and A. Toumar for discussion and support with SCAN calculations.

Author contributions

W.S. and G.C. initiated and supervised the project. M.B. and J.W. designed the experiments. J.W. conducted synchrotron-based measurements with the help of T.S., M.Z., J.B., F.W. and H.K. M.B. and J.W. performed XRD data analysis and Rietveld refinement. R.J.C. and B.O. conducted DFT and reaction energy calculations and analysed the results with the help of D.K. R.J.C. constructed the finite-temperature phase diagram. P.X. carried out the solid-state nudged elastic band calculation. Y.Z. acquired the TEM and EDS data. Y.W. performed phonon frequency calculations. W.S. conceived and calculated the energy cascade with the help of J.W., M.B., J.W., W.S. and G.C. wrote the manuscript.

Competing interests

The authors declare no competing interests.

Additional information

Supplementary information is available for this paper at <https://doi.org/10.1038/s41563-020-0688-6>.

Correspondence and requests for materials should be addressed to W.S. or G.C.

Reprints and permissions information is available at www.nature.com/reprints.